Monthly Notices
of the
ROYAL ASTRONOMICAL SOCIETY

MNRAS **469,** 693–704 (2017)
Advance Access publication 2017 April 8

doi:10.1093/mnras/stx862

AGNs with discordant optical and X-ray classification are not a physical family: diverse origin in two AGNs

I. Ordovás-Pascual,[1]★ S. Mateos,[1] F. J. Carrera,[1] K. Wiersema,[2] X. Barcons,[1] V. Braito,[3] A. Caccianiga,[4] A. Del Moro,[5] R. Della Ceca[4] and P. Severgnini[4]

[1]*Instituto de Física de Cantabria (CSIC-UC), E-39005 Santander, Spain*
[2]*Department of Physics and Astronomy, University of Leicester, Leicester LE1 7RH, UK*
[3]*INAF – Osservatorio Astronomico di Brera, via E. Bianchi 46, I-23807 Merate, Italy*
[4]*INAF – Osservatorio Astronomico di Brera, Via Brera 28, I-20121 Milan, Italy*
[5]*Max-Planck-Institut für Extraterrestrische Physik (MPE), Postfach 1312, D-85741 Garching, Germany*

Accepted 2017 April 5. Received 2017 April 5; in original form 2016 November 11

ABSTRACT

Approximately 3–17 per cent of active galactic nuclei (AGNs) without detected rest-frame UV/optical broad emission lines (type-2 AGN) do not show absorption in X-rays. The physical origin behind the apparently discordant optical/X-ray properties is not fully understood. Our study aims at providing insight into this issue by conducting a detailed analysis of the nuclear dust extinction and X-ray absorption properties of two AGNs with low X-ray absorption and with high optical extinction, for which a rich set of high-quality spectroscopic data is available from *XMM–Newton* archive data in X-rays and XSHOOTER proprietary data at UV-to-NIR wavelengths. In order to unveil the apparent mismatch, we have determined the A_V/N_H and both the supermassive black hole and the host galaxy masses. We find that the mismatch is caused in one case by an abnormally high dust-to-gas ratio that makes the UV/optical emission to appear more obscured than in the X-rays. For the other object, we find that the dust-to-gas ratio is similar to the Galactic one but the AGN is hosted by a very massive galaxy so that the broad emission lines and the nuclear continuum are swamped by the star light and difficult to detect.

Key words: galaxies: active – galaxies: nuclei – galaxies: Seyfert – X-rays: galaxies.

1 INTRODUCTION

The standard unified model of active galactic nuclei (AGNs; Antonucci 1993, Urry & Padovani 1995) explains the observed differences between optical type-1 and type-2 AGNs through orientation effects. If our line-of-sight to the central engine intercepts the nuclear absorber invoked by unified models, the UV/optical continuum emission, the rest-frame UV/optical broad emission lines (line widths $\geq$1500 km s^{-1} in full width at half-maximum, FWHM) and the X-ray emission, originated at sub-parsec scales, should be absorbed. In this case, the AGN is classified as type-2. On the contrary, if we have a direct view of the central engine, UV/optical broad emission lines should be detected, while the X-ray emission should have low absorption ($N_H < 4 \times 10^{21}$ cm^{-2}, the equivalent to $A_V =$ 2 mag using a Galactic dust-to-gas ratio, Caccianiga et al. 2008). In this case, the AGN is classified as type-1.

The classification of AGNs using either the optical range or X-rays should agree according to this model. Nevertheless, approximately 10–23 per cent of AGNs optically classified as type-1 present an X-ray absorbed spectrum (normally with $N_H < 10^{22}$ cm^{-2}), while 3–17 per cent of type-2 AGNs are X-ray unabsorbed (e.g. Panessa & Bassani 2002; Caccianiga et al. 2004; Mainieri et al. 2005; Mateos et al. 2005b,a, 2010; Caccianiga et al. 2008; Corral et al. 2011; Page et al. 2011; Scott, Stewart & Mateos 2012; Merloni et al. 2014). The mismatch between optical extinction and X-ray absorption described above is observed in both optical/infrared-selected and X-ray selected samples at all redshifts. The origin of such apparent discrepancies remains unclear, as well as the validity of the unified model for such AGNs. To unveil the nature of such discrepancies, we need detailed studies on these discordant AGNs.

For X-ray unabsorbed type-2 AGNs, one possibility to explain this discrepancy can be the presence of a Compton-thick absorber (intrinsic N_H equal or larger than the inverse of the Thomson cross-section: $N_H > \sigma_T^{-1} = 1.5 \times 10^{24}$ cm^{-2}). In this case, the direct X-ray emission below 10 keV should be completely suppressed and we would only detect scattered nuclear radiation (Braito et al. 2003, 2011; Akylas & Georgantopoulos 2009; Malizia et al. 2012). Since the scattered emission is only 1–3 per cent of the intrinsic AGN emission (Gilli, Salvati & Hasinger 2001;

★ E-mail: ordovas@ifca.unican.es

Comastri 2004; Georgantopoulos et al. 2011b), the sources would be identified as low-luminosity, unabsorbed type-2 AGNs. Another possibility is that the broad UV/optical lines are diluted by the host galaxy emission (Severgnini et al. 2003; Georgantopoulos & Georgakakis 2005; Caccianiga et al. 2007, 2008). An alternative explanation could be a high dust-to-gas ratio: normally, AGNs show dust-to-gas ratios below the Galactic standard or comparable ratios (Maiolino et al. 2001; Vasudevan et al. 2009; Parisi 2011; Marchese et al. 2012; Hao et al. 2013; Burtscher et al. 2016), if this ratio is substantially higher, significant suppression of the broad-line emission could take place without strong effects in the X-ray bands. Dust-to-gas ratios well above the Galactic value have been found in some AGNs, although such cases are rare (Caccianiga et al. 2004; Trippe et al. 2010; Huang et al. 2012; Malizia et al. 2012; Masetti et al. 2012; Mehdipour, Branduardi-Raymont & Page 2012). In the sample of Maiolino et al. (2001), a sample of AGNs whose X-ray spectrum shows cold absorption and whose optical and/or IR spectrum show at least two broad lines, this is found in 9 per cent of the sources, and in the HBS28 sample (Caccianiga et al. 2004) this is only found in 3 per cent. In other objects, optical observations show an intrinsically high Balmer decrement for the hydrogen broad emission lines, while the X-ray spectra show low absorption (Barcons, Carrera & Ceballos 2003). A dusty-ionized absorber like the one in NGC 7679 (Della Ceca et al. 2001) can produce more relative absorption in the X-rays than in the optical emission. One last possible explanation is a variability scenario since optical and X-ray observations are normally obtained at different epochs. However, we note that, even with simultaneous observations, there are some objects whose optical and X-ray classification do not match (Bianchi et al. 2008, 2012; Corral et al. 2015).

The objective of this study is to get insight into the physics behind the apparent mismatch between UV/optical and X-ray classification of two low-z AGNs selected from the Bright Ultra-hard *XMM–Newton* Survey (BUXS, Mateos et al. 2012): 2XMMiJ000441.2+000711 (hereafter J00, $z = 0.1075$, Abazajian et al. 2009) and 2XMMJ025218.5−011746 (hereafter J02, $z = 0.0246$, Jones et al. 2009). While both sources appear unabsorbed in X-rays, J00 has been optically classified as type-1.9 using the SDSS-DR7 spectrum (Abazajian et al. 2009) and J02 is a Sb edge-on galaxy (de Vaucouleurs et al. 1991) optically classified as a type-2 AGN (6dF spectrum, Jones et al. 2009).

For these sources, we obtained UV-to-NIR XSHOOTER spectra (PI: S. Mateos) and by comparing the properties derived in X-rays and in the UV/optical, we have tested three possible scenarios to explain the discordance: (a) the presence of a Compton-thick AGNs; (b) these sources are a normal AGN but in a very massive host galaxy, or weak AGNs in a normal host galaxy and their broad UV/optical emission lines are diluted by the host galaxy emission; (c) intrinsic non-standard nuclear properties, such as a high dust-to-gas ratio or an intrinsically weak broad-line region (BLR).

This paper is organized as follows. In Section 2, we explain how our objects are selected. In Section 3, we describe the *XMM–Newton* data and in Section 4 we describe the XSHOOTER observations. In Section 5, we derive the AGN emission by subtracting the host galaxy emission, as well as the AGN intrinsic reddening, its emission lines and the host galaxy properties. We finally discuss all the possible contributions that can cause a mismatch between the X-ray and UV/optical properties of our objects in Section 6. Throughout this paper errors are 1σ. We assume a Λ cold dark matter cosmology with $\Omega_{\rm M} = 0.3$, $\Omega_{\Lambda} = 0.7$ and $H_0 = 70\,{\rm km\,s^{-1}\,Mpc^{-1}}$.

2 THE SAMPLE

The two AGNs analysed in this work were selected from the wide-angle (44.43 deg^2) BUXS (Mateos et al. 2012). This is a flux-limited sample of 255 AGNs detected in the 4.5–10 keV band with the *XMM–Newton* observatory. The objects have relatively bright X-ray fluxes $f_{4.5-10\,{\rm keV}} \geq 6\times\ 10^{-14}$ erg s^{-1} cm^{-2}. At the time of writing, the optical spectroscopic identification completeness is >98 per cent. There are 111 AGNs in BUXS with optical spectroscopic classifications 1.8, 1.9 or 2. Of these, nine objects showing low X-ray absorption ($N_{\rm H} < 4 \times 10^{21}$ cm^{-2}; Caccianiga et al. 2008) that are visible from Paranal were included in a proposal for follow-up with XSHOOTER. Only two objects with the lowest declination were successfully observed with XSHOOTER. We discuss here in detail the properties of these two objects.

For both sources, we have proprietary high-resolution UV-to-NIR XSHOOTER spectra, as well as good quality *XMM–Newton* X-ray spectra (Jansen et al. 2001) in the observed energy range from 0.25 to 10 keV (Table 1 and Fig. 1).

3 X-RAY PROPERTIES

Source and background spectra were extracted at energies from 0.25 to 10 keV using circular regions. We used the *XMM–Newton* Science Analysis System (SAS) task `eregionanalyze` to obtain the circles that maximized the signal-to-noise ratio. For J00, we used radii of 34 and 32 arcsec for the MOS (Strüder et al. 2001) and pn (Turner et al. 2001) cameras, respectively. For J02, we used a radius of 29 arcsec for MOS and 25 arcsec for pn. The background spectra were extracted using circular regions of 50 arcsec radius located in source free regions in the same CCD chip as our objects. The response matrices and effective area curves were obtained using the SAS tasks `rmfgen` and `arfgen`, respectively. We combined MOS1 and MOS2 source and background spectra and the corresponding response matrices. The spectra were grouped with a minimum of 15 counts per bin and are shown in Fig. 1.

The X-ray spectroscopic analysis was conducted with the XSPEC package (v12.9.1; Arnaud 1996). We fitted the spectra with a combination of different models to determine the shape of the direct and scattered broad-band continuum components (modelled with power laws), soft excess (modelled with a blackbody) and rest-frame line-of-sight X-ray absorption. The models take into account the Galactic absorption using column densities taken from Dickey & Lockman (1990). We fitted both the pn and MOS spectra at the same time with the parameters of the model tied, except for the continuum normalization to take into account cross-calibration problems between MOS and pn cameras (Mateos et al. 2009).

To accept the detection of a model component, we used the F test with a significance threshold of 95 per cent. The X-ray luminosities have been computed in the rest-frame 2–10 keV energy band. They are corrected for X-ray Galactic absorption and the X-ray intrinsic absorption of the sources.

J00: it is X-ray unabsorbed. The 1σ upper limit on the column density is 6.7×10^{20} cm^{-2}. The best-fitting model is a combination of a blackbody with temperature $kT = 0.16^{+0.01}_{-0.02}$ keV and an unabsorbed power law with photon index $\Gamma = 1.66 \pm 0.09$. The X-ray spectra (MOS and pn) are shown in Fig. 1 (left). For a sanity check, we computed the X-ray absorption with a fixed photon index of $\Gamma = 1.9$, the typical value for type-1 AGNs (Caccianiga et al. 2004; Galbiati et al. 2005; Mateos et al. 2005a,b, 2010; Tozzi et al. 2006; Corral et al. 2011). We still classify this object as a low-absorption AGN ($N_{\rm H} \leq 1.3 \times 10^{21}$ cm^{-2}). The blackbody emission

Table 1. X-ray information about the selected objects.

Object (1)	z (2)	Obs. ID (3)	T. exp (4)	Cts (5)	Flux (6)	log(L) (7)	$N_{\rm H}$ (8)	$N_{\rm H,\,G}$ (9)	Γ (10)	kT (11)	Model (12)	χ^2/dof (13)
		0305751001	26 574	1172								
J00	0.1075	(2005-12-10)	(11 476)	(1318)	2.04 ± 0.22	42.76 ± 0.05	<0.67	0.31	1.66 ± 0.09	$0.16^{+0.01}_{-0.02}$	*bb+po*	169.2/139
		0151490101	55 203	830								
J02	0.0246	(2003-07-16)	(22 017)	(866)	$1.31^{+1.07}_{-0.99}$	41.25 ± 0.03	$1.7^{+2.0}_{-1.4}$	0.51	2.08 ± 0.09	–	*apo*	135.1/100

Notes. (1) J00 = 2XMMiJ000441.2+000711, J02 = 2XMMJ025218.5−011746. X-ray source identifier as listed in the Second *XMM–Newton* Serendipitous Source Catalogue (2XMM-DR3; Watson et al. 2009; http://xmmssc-www.star.le.ac.uk/Catalogue/xcat_public_2XMMi-DR3.html). (2) Redshift. (3) *XMM–Newton* Observation ID. In brackets we show the date of the observation. (4) Observation exposure time in seconds after removal of high background flares in MOS1+MOS2 and in pn in brackets. (5) Net counts of the MOS spectra between 0.25 and 10 keV and pn spectra between 0.25 and 10 keV, the latter in brackets. (6) 2–10 keV flux in units of 10^{-13} erg cm^{-2} s^{-1}. (7) Logarithm of luminosity in the 2–10 keV range corrected for extinction. (8) Best-fitting X-ray column density in units of 10^{21} cm^{-2}. (9) Galactic column density from the Dickey and Lockman H I map (Dickey & Lockman 1990) in units of 10^{21} cm^{-2}. (10) Power-law photon index. (11) Temperature of the blackbody. (12) Best-fitting model, where *bb+po* stands for blackbody emission plus a power law, and *apo* stands for an absorbed power law. All reported errors are at the 1σ level.

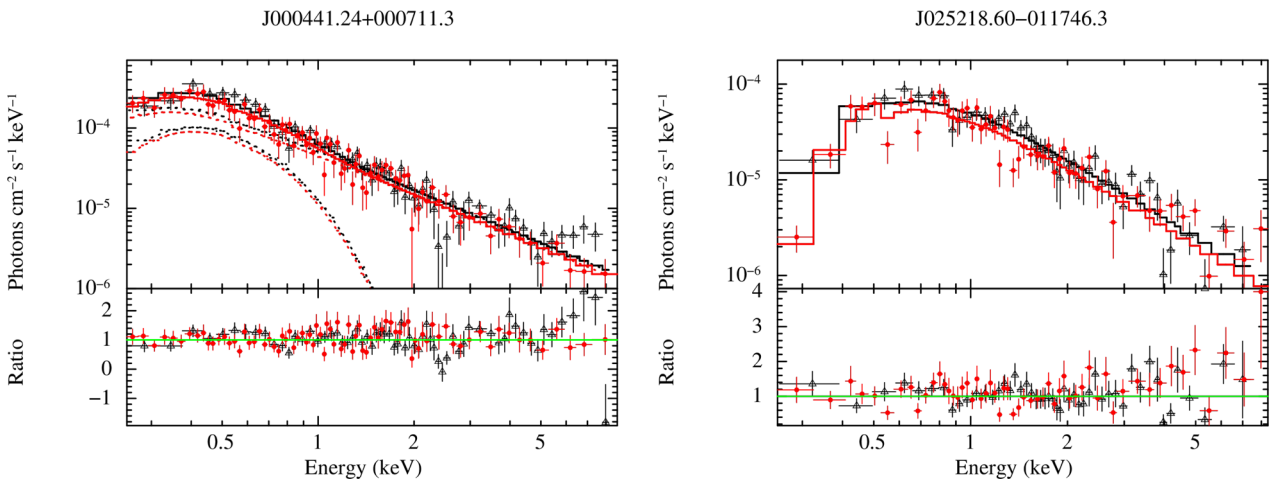

Figure 1. Left: MOS (black triangles) and pn (red dots) spectra of J00 and the best-fitting model (blackbody + power law) in solid lines. Each component of the X-ray model is plotted with dotted lines. Right: MOS (black) and pn (red) X-ray spectra of J02 and the best-fitting model (absorbed power law) in solid lines. We also represent the ratio between the data and the best-fitting model.

is a phenomenological model often used in the literature (Corral et al. 2015) to fit the soft X-ray excess. Nevertheless this is not physically correct for J00, as it is well known that the temperature of the blackbody for a supermassive black hole (SMBH) such as the one for J00 (see Section 5.3) is too low to explain the soft X-ray excess. We also tried a more physically motivated model, albeit more complex, replacing the blackbody model with a hot diffuse gas model (`mekal` model in XSPEC; Mewe, Gronenschild & van den Oord 1985; Mewe, Lemen & van den Oord 1986; Kaastra 1992; Liedahl, Osterheld & Goldstein 1995). This gives us an upper limit on the column density of 2.4×10^{20} cm^{-2} (with $\Gamma = 1.83 \pm 0.07$, χ^2/dof = 173.7/139). The results, in terms of the X-ray classification as absorbed/unabsorbed, do not change using one model or the other. Therefore, we use in this paper the results with the blackbody since we obtain a more conservative value of $N_{\rm H}$. The equivalent width of the Fe line at 6.4 keV in the rest frame is formally equivalent width (EW) $= 0.30^{+0.16}_{-0.17}$ keV, but adding this line is not statistically significant ($\Delta\chi^2 = 3$ for Δdof = 1, a 1.73σ detection). Looking at the spectrum of J00 (Fig. 1), we can see a bump at the hard energies, but we believe that is not real, since it is only present in one of the EPIC cameras. This feature is probably associated with residuals in the background subtraction. Nevertheless, since the shape of the continuum is very well determined by the values at lower energies, this is not affecting our best-fitting estimates.

J02: the best-fitting model is an absorbed power law with photon index $\Gamma = 2.08 \pm 0.09$ and intrinsic $N_{\rm H} = 1.7^{+2.0}_{-1.4} \times 10^{21}$ cm^{-2}. The EW of the Fe line is formally EW $= 1.12^{+0.49}_{-0.39}$ keV, that is strong, but the detection is not significant ($\Delta\chi^2 = 6$ for Δdof = 1, a 2.45σ detection).

4 UV-TO-NIR OBSERVATIONS

We have obtained UV-to-NIR high-resolution spectra for both objects at the Very Large Telescope (VLT) with the VLT/XSHOOTER instrument (Vernet et al. 2011). The instrument divides the light in three paths that lead to three arms: one for the UV light, the second for the visible light and the last one for the near-infrared (UVB, VIS and NIR, respectively). Each arm disperses the light with an echelle grating. The observations were taken with a 1.0arcsec × 11arcsec slit for the UVB arm and 0.9arcsec × 11arcsec slits for the VIS and NIR arms, respectively. Table 2 shows some technical details of the configuration set-up of the observations.

The spectra were taken in nodding mode. In Table 3, we show some information about the spectra acquisition. We present in Fig. 2 the acquisition images of both objects and indicate the slit projected in the sky, the extraction region of the spectra and the parallactic angle. The observation dates were 2010-09-07 for J00 and 2010-09-04 for J02.

Table 2. XSHOOTER observing configuration set-up.

Arm (1)	Slit (2)	R (3)	Inst. Br. (4)	T_{exp} (5)	Range (6)
UVB	1.0	4350	0.86 ± 0.20	1420	3000–5500
VIS	0.9	7450	1.14 ± 0.25	1420	5500–10 000
NIR	0.9	5300	0.88 ± 0.08	2×480	10 000–25 000

Notes. (1) Instrument arm. (2) Slit width in arcsec. (3) Spectral resolution $R = (\lambda/\delta\lambda)$ according to the XSHOOTER webpage.[2] (https://www.eso.org/sci/facilities/paranal/instruments/xshooter/inst.html). (4) Instrumental broadening in Å, measured using arc lines. (5) Exposure time in s. (6) Wavelength coverage of each arm in Å.

Table 3. XSHOOTER spectra acquisition information.

Object (1)	Date (2)	Nodding (3)	Airmass (4)
J00	2010-09-07	+2.5 arcsec −2.0 arcsec	1.14
J02	2010-09-04	+2.5 arcsec −1.5 arcsec	1.09

Notes. (1) Object. (2) Observation date (YYYY-MM-DD). (3) Nodding separation in arcsec. (4) Airmass.

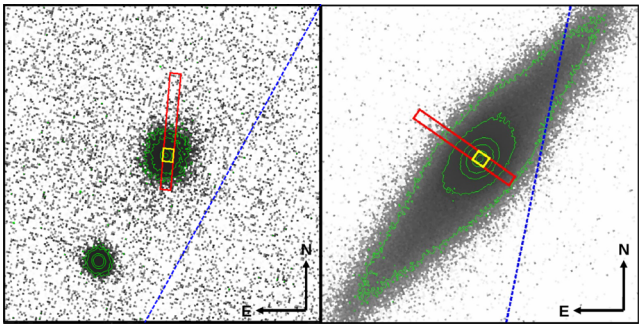

Figure 2. Section of 0.5arcmin × 0.5arcmin of the acquisition image of J00 (left) and J02 (right) with the projection of the slit in the red box, 1arcsec × 11arcsec, for one of the nodding positions. Both images were taken with the *i*-band filter. The small yellow box inside the slit is the extraction region of the spectrum, 1 arcsec × 1.22 arcsec. The blue dashed line represents the parallactic angle. In green, we plot contours of the objects. For J00, we plot 5, 10, 50 and 90 per cent contour levels with respect to the peak of the AGN emission, and in J02 we plot the same contour levels plus an additional 2 per cent one.

XSHOOTER is equipped with an atmospheric dispersion correction (ADC) that allows the acquisition of the spectrum using any angle at any position in the sky. During our observations, the ADC was functional. For J02, we positioned the slit at an inclination angle close to the minor axis of the host galaxy to allow sky subtraction. Thanks to the ADC we could choose an inclination angle closer to the minor axis of the host galaxy. The observations were taken close to the meridian and with low air mass, meaning that the effect of the atmospheric dispersion is small.

The observations were reduced using the public XSHOOTER pipeline version 2.3.0 with Gasgano, following the instructions described in the XSHOOTER pipeline manual.[1] We used a binning in the wavelength direction 0.02 nm pixel^{-1} for the UVB and VIS arms and 0.06 nm pixel^{-1} for the NIR arm, and in the slit direction 0.16 arcsec pixel^{-1} for the UVB and VIS arms and 0.21 arcsec pixel^{-1} for the NIR arm, as specified in the XSHOOTER user manual. We used the standard procedures in the pipeline. IRAF Laplacian Cosmic Ray Identification task for spectroscopy (`lacos_spec`, van Dokkum 2001) was applied to the raw images for cosmic ray rejection and then each arm was reduced individually. We used the standard star GD71 (RA = 05:52:27.61, Dec. = +15:53:13.8) to calibrate the flux of our spectra. There are three different recipes to do the flux calibration: the offset mode, the staring mode and the nodding mode. We used the recipe for the staring mode, as it provides a better background subtraction. We used the software IRAF to extract the 1D spectra being careful to follow the trace. This was carried out with the routine `apall`. This is because the spectra have a trace whose centre was not constant in the cross-dispersion direction due to an imperfect order rectification of the pipeline.

We joined the spectrum from each XSHOOTER arm following the information about the dichroic crossover region in the XSHOOTER user manual. To join the UVB and VIS arms, the crossover region is at 5595 Å, while between the VIS and NIR it is at 10 140 Å. The transition regions are 5560–5638 and 10 095–10 350 Å, respectively. A 0.9–1.1 scaling factor between arms is sometimes needed to match in flux the complete spectrum (López et al. 2016; Nisini et al. 2016). We used the continuum in these regions around the crossover points to compute the flux scaling factors for each arm using the VIS one as reference. We scaled the UVB arm spectra using a factor of 0.9 while for the NIR arm a 1.0 flux scaling factor was acceptable. Errors were propagated through this process.

The aperture used to extract the spectra was defined to maximize the signal to noise of the AGN emission. This was carried out using the software IMFIT[2] on the acquisition images of the VLT observations. Both images were taken using the *i*-band filter. In both targets, a bright nuclear source was detected (see contours in Fig. 2). To compute the fraction of the AGN light that enters through the slit, for J00 we decomposed the emission in a Gaussian function for the AGN, and a Sérsic profile for the host galaxy. J02 is an edge-on galaxy so we used a Gaussian profile for the AGN and two Sérsic profiles for the host galaxy, to fit the bulge and the disc. The parameters of the Sérsic and Gaussian models (intensity, σ, effective radius, Sérsic index) are computed with errors of ∼20 per cent or less, indicating reliable fits of the photometric images. In Fig. 2, the contours show that we have enough quality to fit the shape of the different components of our objects. We can trust the reliability of the acquisitions images to measure the slit losses using the width of the Gaussian profiles which are ∼2.5 and ∼3.5 pixels for J00 and J02, respectively.

We estimated that about 75 per cent and 56 per cent of the AGN emission are included in the slit for J00 and J02, respectively.

The reduction of the science spectra is concluded by correcting for Galactic extinction, putting the wavelength and flux in rest frame and converting the air wavelengths into vacuum wavelengths. Information to perform these corrections was obtained from the public data available in NASA/IPAC Extragalactic Database.

5 ANALYSIS

In this section, we describe the steps carried out to isolate the AGN emission in the XSHOOTER spectra and to determine the properties of the AGN and their host galaxies.

[1] ftp://ftp.eso.org/pub/dfs/pipelines/xshooter/xshoo-pipeline-manual-12.2.pdf

[2] http://www.mpe.mpg.de/∼erwin/code/imfit/

5.1 AGN and host galaxy continuum decomposition

To decompose the extracted spectra into AGNs and host galaxy emission at UV-to-NIR wavelengths, we used the software STARLIGHT (Cid Fernandes et al. 2005; Mateus et al. 2006).The best-fitting model was obtained by minimizing the χ^2 statistic. We modelled the spectra with a composite model including a host galaxy spectrum plus an absorbed (by nuclear and host galaxy extinction) AGN spectrum. To reduce noise and to follow the recommendations of the STARLIGHT manual, we rebinned the spectrum to 2 Å bins. spectral energy distributions (SED) decomposition is an approach commonly used to compute the relative contributions from the AGNs and their hosts. Nevertheless, both the good spectral resolution and wide wavelength coverage of the X-SHOOTER spectra allow us to calculate the AGNs and stellar components without resorting to a full SED decomposition.

We need to assume a spectral shape for the rest-frame UV to near-IR AGN continuum. There is substantial scatter in the continuum shapes of individual AGN which also depend on the SMBH mass and can vary with time (Koratkar & Blaes 1999; Schmidt et al. 2012; Baron et al. 2016). Since our aim is to reproduce the intrinsic AGN continuum by finding the model that best fits each source, we have adopted the broken power law models ($F_\lambda \propto \lambda^\alpha$) from Polletta et al. (2007). In these models, the spectral index ranges from $\alpha = -1.9$ to -1.4 for $\lambda < 10000$ Å and $\alpha = -0.8$ to -0.6 redwards, and the break is located at 10 000 Å. This break is likely associated with the change in the AGN continuum slope between the IR bump and the big blue bump (Koratkar & Blaes 1999). We used this information to create a set of broken power laws with the previously mentioned index range to reproduce the intrinsic AGN continuum emission of our objects. The steps in the power-law index to create the grid of broken power-law models are $\Delta\alpha = 0.125$ for the blue region and $\Delta\alpha = 0.05$ for the red.

The next parameter needed in our fit is the obscuration of the nuclear region of the AGN. We used the extinction model of the Small Magellanic Cloud (SMC; Gordon et al. 2003) as it is the one that fits the AGN spectra better (Hopkins al. 2004). We tried different extinction models but the SMC is the one that minimized χ^2. In particular, we checked the Large Magellanic Cloud Super-Shell and Average models from Gordon et al. (2003), the Calzetti et al. (2000) law, the Milky Way model form Allen (1973) and the model from Cardelli, Clayton & Mathis (1989). In addition, using the SMC model we obtained the most conservative A_V values. We constrained the nuclear extinction to be between $A_V = 10$ and 0 mag.

The host galaxy contribution is modelled using the single stellar population (SSP) templates from the Bruzual & Charlot (2003) library. We used 45 models with metallicities $Z = 0.05$, 0.02 and 0.004 in units of the solar value and ages ranging from 1 Myr to 13 Gyr. We obtained SSP in the 0.8–13 Gyr range for our objects.

In order to fit the AGN and host galaxy continuum emission only, we masked out the spectral ranges where the AGN emission lines and the telluric absorption lines are expected (see grey and yellow bands in Fig. 3). We excluded the regions between 6850–6950, 7165–7210 and 7550–7725 Å, where some residuals of telluric features in the Bruzual and Charlot library are present.

The final spectral range used in the fit is between 3700 and 16000 Å (rest frame).

Fig. 3 shows the results of the spectral decomposition. We see that in both objects, the total emission is dominated by the host galaxy. The preferred models are $\alpha_{blue} = -1.90$ and $\alpha_{red} = -0.6$ for J00 and for J02 $\alpha_{blue} = -1.78$ and $\alpha_{red} = -0.6$. The resulting values of intrinsic absorption associated to the AGN emission are $A_V = 2.04 \pm 0.30$ mag and $A_V = 2.19 \pm 0.33$ mag for J00 and for J02, respectively.

We computed the errors in the extinction by varying the power-law index and then fitting again and calculating the χ^2 statistics. The errors obtained are very small. We added an additional 15 per cent error contribution to account for the overall uncertainty of the SMC model used (Gordon et al. 2003). This contribution to the error is the one that dominates.

We believe that the results from the AGN and host galaxy decomposition reported in this section are robust. The XSHOOTER spectra have a sufficiently large wavelength range to constrain in a robust way the host galaxy contribution, which is the major contribution at optical wavelengths. It is clear that in the spectra there are several stellar features that help constraining the emission from the hosts (see Fig. 3). If more relative contribution of the nuclei is present in the spectra, this would in fact flatten the stellar features to a more featureless contribution. The STARLIGHT software fits this stellar features and the results in this paper are the best-fitting ones.

5.2 Narrow-line and broad-line Balmer decrements

After removing the host galaxy component and after having taken into account the slit losses, we estimated the Balmer decrement by using the broad and narrow components of the H α and H β emission lines.

We fitted the nuclear spectra from rest-frame 6270 to 6800 Å for H α. For the H β region we fitted from rest-frame 4600 to 5050 Å for J00 and from 4800 to 5050 Å for J02. We used a wider wavelength range in the first object to ensure fitting the whole broad H β emission line. To model the AGN narrow emission lines we used Gaussian functions, assuming that they share the same width in velocity space. Hydrogen broad emission lines are fitted with Gaussian profiles as well. We included also a parameter for the broad line that is a shift of the centre of the Gaussian with respect to the vacuum values. This is because some AGNs show broad lines with an offset, sometimes of a thousand of km s^{-1} due to strong winds (Sulentic, Marziani & Dultzin-Hacyan 2000; Steinhardt et al. 2012; Gaskell & Goosmann 2013). For J00, the shift is $\sim$30 Å ($\sim$1350 km s^{-1} in velocity) while for J02 is $\sim$3 Å ($\sim$150 km s^{-1}), not unusual with respect to the observed shifts (Sulentic et al. 2000). We used a power law to fit the continuum around the lines. The line parameters were obtained with the CIAO's SHERPA fitting tool (Freeman, Doe & Siemiginowska 2001).

Since the broad H β component was not detected in any of the spectra, only an upper limit could be computed for the Balmer decrement from the BLR. Line parameters and Balmer decrements are reported in Table 4. The narrow-line Balmer decrement will be compared in Section 6.3 with the absorption in the X-rays and the extinction of the UV-to-NIR continuum.

In Fig. 4, we show our results while best-fitting values are indicated in Table 4.

5.3 SMBH masses

From the XSHOOTER nuclear spectra, we derived an estimate of the SMBH masses for our targets. There are many different ways to compute SMBH masses (Trippe 2015). We used the luminosity and FWHM of the H α broad emission line and the expression from

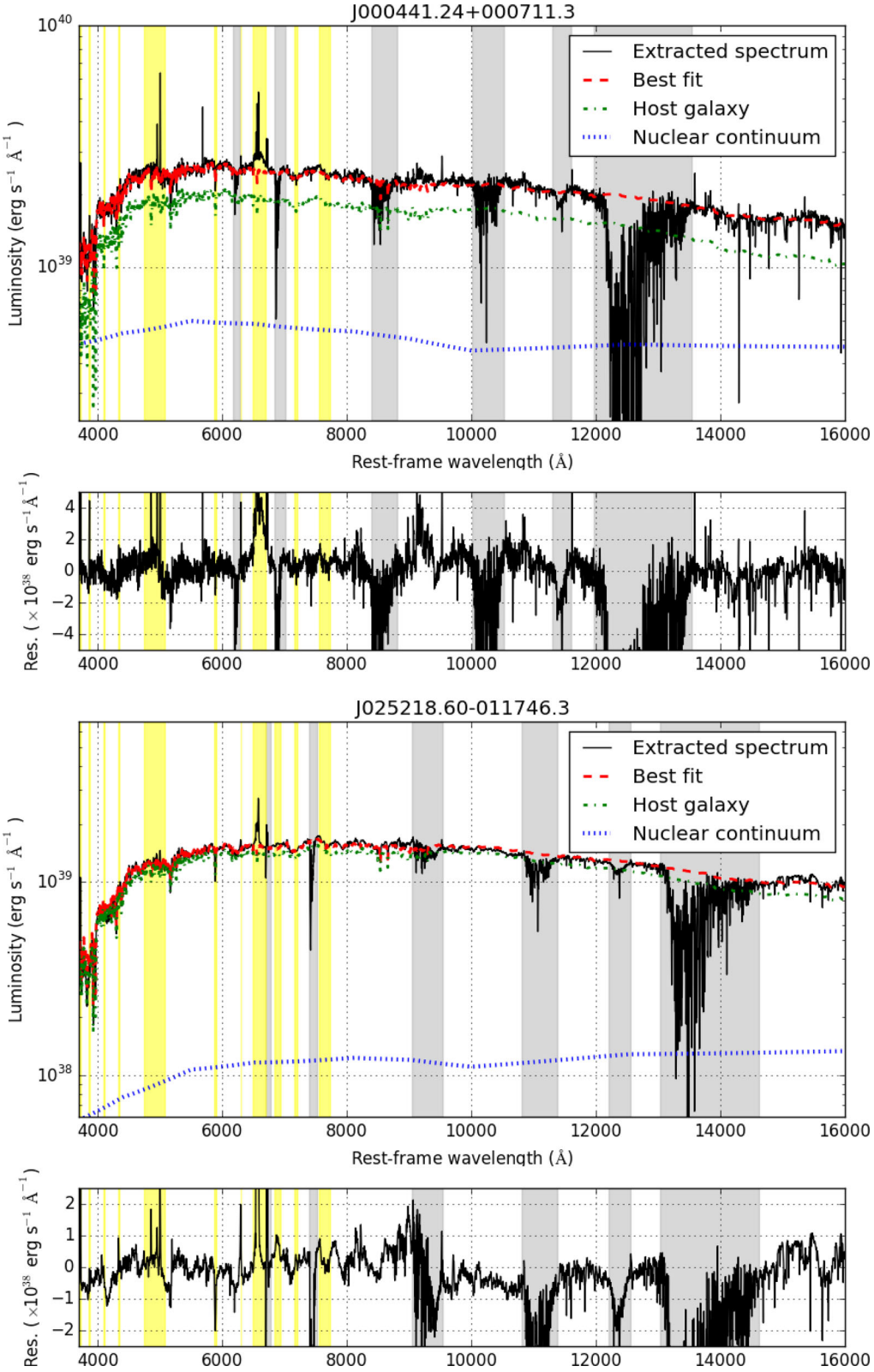

Figure 3. Decomposition of the UV-to-NIR spectra of J00 (top) and J02 (bottom) into host galaxy and AGN components. The upper panels represent the results of the fits while the bottom panels show the residuals. The grey and yellow bands indicate the telluric absorption features and the spectral regions with AGN emission lines, respectively, which are ignored in the fits.

Table 4. AGN fitting results.

	J00	J02
$\log(M_{\rm SMBH}/{\rm M}_\odot)$	$7.96^{+0.23}_{-0.25}$	$6.74^{+0.26}_{-0.22}$
$\rm FWHM_{H\,\alpha,B}$	7830 ± 1221	2499 ± 175
$\rm FWHM_{H\,\alpha,N}$	246 ± 19	376 ± 17
$L_{\rm H\,\alpha,B}$	22.0 ± 2.0	6.15 ± 0.61
$L_{\rm H\,\alpha,N}$	2.63 ± 0.13	0.52 ± 0.08
$L_{\rm H\,\beta,B}$	≤ 16.2	≤ 1.51
$L_{\rm H\,\beta,N}$	$0.89^{+0.19}_{-0.21}$	0.17 ± 0.03
$L_{\rm [O\,III],\,5008\,\AA}$	$8.37^{+0.49}_{-0.62}$	$0.81^{+0.8}_{-0.12}$
$L^o_{\rm H\,\alpha,N}/L^o_{\rm H\,\beta,N}$	$4.41^{+0.92}_{-1.34}$	$3.34^{+0.80}_{-1.05}$
$L^o_{\rm H\,\alpha,B}/L^o_{\rm H\,\beta,B}$	≥ 3.13	≥ 11.40
$L_{\rm bol}$	1192 ± 118	243 ± 30
$L_{\rm Edd.}$	$1.19^{+0.97}_{-0.56} \times 10^6$	$0.071^{+0.052}_{-0.036} \times 10^6$
$L_{\rm bol}/L_{\rm Edd.}$	$0.0010^{+0.0004}_{-0.0010}$	$0.0034^{+0.0011}_{-0.0034}$

Notes. SMBH masses [in $\log(M_{\rm SMBH}/{\rm M}_\odot)$ units] and properties of the different broad and narrow emission lines used in our analysis. The FWHM is in km s^{-1}. All luminosities are in units of 10^{40} erg s^{-1}. The Balmer decrement, as indicated in the text, is calculated using the reddened AGN spectrum. All luminosities are extinction corrected, except those with the superindex 'o'.

Greene & Ho (2005),

$$\log\left(\frac{M_{\rm SMBH}}{{\rm M}_\odot}\right) = (0.45 \pm 0.05)\log\left(\frac{L_{\rm H\,\alpha}}{10^{42}\,{\rm erg\,s^{-1}}}\right) + (2.06 \pm 0.06)\log\left(\frac{\rm FWHM_{H\,\alpha}}{10^3 {\rm kms^{-1}}}\right) + 6.40^{+0.09}_{-0.07}, \quad (1)$$

where $M_{\rm SMBH}/{\rm M}_\odot$ is the mass of the SMBH in solar units. $L_{\rm H\,\alpha}$ is the intrinsic luminosity of the H$\,\alpha$ emission line in erg s^{-1}, this is, corrected for both the nuclear and the host galaxy extinction, computed from the spectral fits. Finally $\rm FWHM_{H\,\alpha}$ is the FWHM of the broad H$\,\alpha$ emission line in km s^{-1}. We also have corrected the FWHM of the lines by the instrumental spectral dispersion by subtracting the instrumental broadening in quadrature.

We show the SMBH masses computed using equation (1), as well as the relevant luminosities, in Table 4. In addition, we show the bolometric and Eddington luminosities for our sources, as well as the Eddington ratio ($L_{\rm bol}/L_{\rm Edd.}$). The bolometric luminosities are calculated using the expression $L_{\rm bol} = 9\times\,\lambda L_{5100}$ (Kaspi et al. 2000), being L_{5100} the monochromatic luminosity of the unreddened nuclear emission at rest-frame 5100 Å. The Eddington ratio is within the expected values for nearby AGNs with similar bolometric luminosities and SMBH masses (Panessa et al. 2006).

5.4 Host galaxy masses

It is well known that the SMBH mass and the spheroidal mass of the host galaxies follow a linear relation (Merritt & Ferrarese 2001; Park et al. 2012). In this study, we calculate both the dynamical mass and the stellar mass from the spheroidal component of the host galaxy.

5.4.1 Stellar masses

STARLIGHT provides stellar masses for its best-fitting models. We have corrected those for slit losses using the spheroidal components obtained by IMFIT (see Section 4): the fractions of the spheroid light that went through the slit are 9.0 and 6.2 per cent for J00 and J02, respectively.

The stellar mass derived using STARLIGHT is computed using mass-to-light relations, converting each SSP contribution to stellar mass. STARLIGHT does not compute errors in the best-fitting values. In Bell & de Jong (2001), the stellar mass-to-light ratio and the uncertainties associated with this ratio are discussed. This uncertainties are all of the order of 0.1–0.2 dex. We use the largest value as the error for our values to be conservative. Our results are shown in Table 5.

5.4.2 Dynamical masses

As a sanity check, we also computed the dynamical mass of the spheroidal component of the host galaxies. We used the relation between the line-of-sight velocity dispersion ($\sigma_{\rm e}$) and the dynamical mass.

The observed width of the Na I doublet at rest-frame $\lambda\lambda$5896, 5890 (Na ID) is a stellar absorption feature that can be used to calculate $\sigma_{\rm e}$ (Spiniello et al. 2012). The Na ID feature is a convolution of the resolution of the instrument, the intrinsic width of the stellar population and $\sigma_{\rm e}$. To compute $\sigma_{\rm e}$, we used the instrumental resolution from Table 2. For the stellar population, we used the SSP template from the Bruzual and Charlot 2003 library (Bruzual & Charlot 2003) that based on the results of STARLIGHT, is the most dominant SSP for each host galaxy: the SSP of 0.9 Gyr and $Z = 0.05$ for J00, and 11 Gyr and $Z = 0.02$ for J02. The standard dispersion of the Gaussian function gives the desired $\sigma_{\rm e}$.

In Fig. 5, we show the Na ID and the results of the fits. We plot in this figure the template used in each object with the spectral resolution at the region of the doublet. The spectral resolution is computed using the FWHM of the closest arc line of the XSHOOTER observation. To calculate the dynamical mass of our AGN hosts, we used the virial relations from Cappellari et al. (2006) and Taylor et al. (2010).

$$M_{\rm dyn} = k(n) \times \frac{r_{\rm e}\sigma_{\rm e}^2}{G}, \quad (2)$$

where $r_{\rm e}$ is the effective radius of the spheroidal mass of the host galaxy, $\sigma_{\rm e}$ is the line-of-sight velocity dispersion, the factor $k(n)$ that depends on the Sérsic index and G is the universal gravitational constant. Using the software IMFIT we obtained $r_{\rm e}$ and the Sérsic index by fitting the acquisition images from the VLT. To compute the error in the spheroidal mass we propagate errors.

We summarize in Table 5 the properties of our AGN hosts. We clearly see that our dynamical mass estimates are compatible with the stellar masses calculated before. The studied galaxies are massive but not atypical (Vitale et al. 2013).

6 DISCUSSION

In the following subsections, we discuss one by one the possible causes of the apparent discordant properties of our AGNs in the UV/optical range and in X-rays.

6.1 Compton-thick or Compton-thin obscuration

Based on the observed X-ray properties, we can rule out that our objects are Compton-thick. First of all the broad-band continuum shape is too steep to be produced mainly by reflected emission as demonstrated in Section 3. Compton-thick sources usually have $\Gamma \sim 1.0$ (Brightman et al. 1999; Winter et al. 2008; Georgantopoulos et al. 2011a; Del Moro et al. 2016).

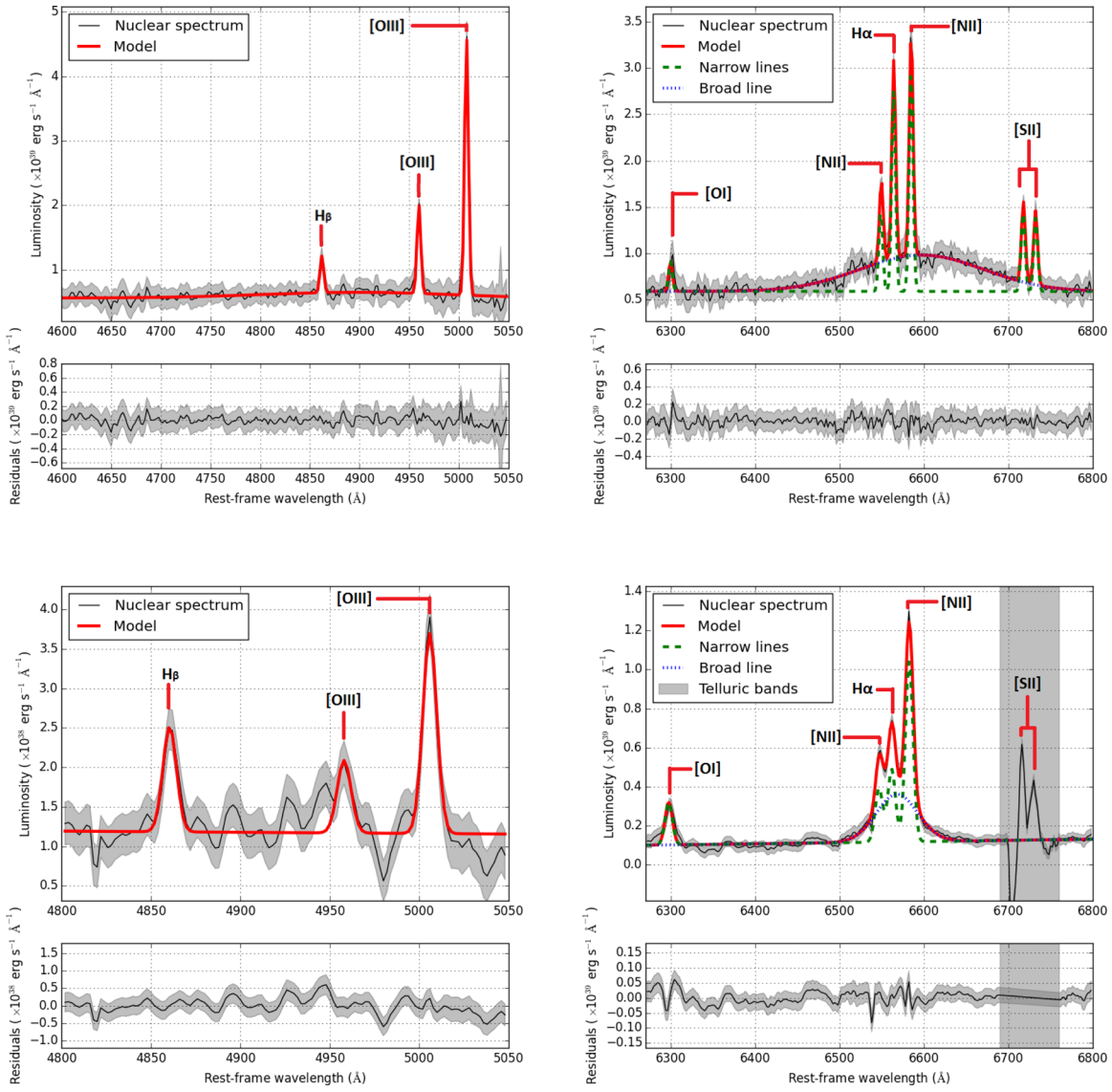

Figure 4. Top: decomposition of the AGN emission into continuum plus narrow and broad emission lines for J00 (top) and J02 (bottom). Left-hand panels: H β+[O III] region. Right-hand panels: H α region. In grey, we plot the error of each spectrum. We also indicate the observed narrow emission lines.

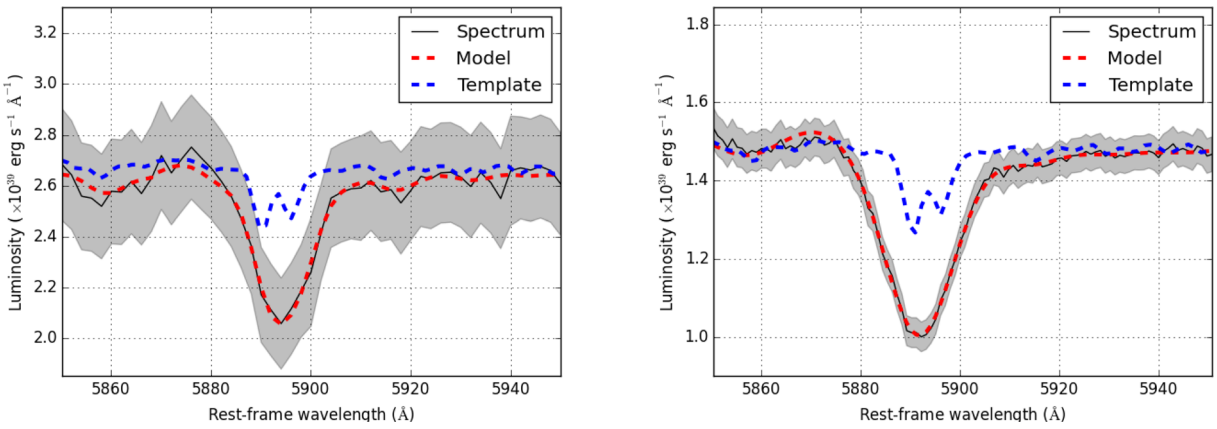

Figure 5. Spectrum (in black) of the Na I Doublet of J00 (left) and J02 (right) and its fit (in red). In grey we show the error of each spectrum. In blue we plot the template used to measure σ_e in the region of Na ID. The template has a spectral resolution of 1.28 Å.

Table 5. Host galaxy properties.

	J00	J02
σ_e	145 ± 109 km s^{-1}	260 ± 87 km s^{-1}
r_e	4.21 ± 0.39 kpc	0.84 ± 0.04 kpc
n	1.17	0.96
$k(n)$	7.92	7.96
$\log(M_{dyn}/M_\odot)$	$11.07^{+0.23}_{-0.42}$	$10.85^{+0.11}_{-0.12}$
$\log(M_{stell}/M_\odot)$	$10.73^{+0.20}_{-0.20}$	$10.89^{+0.20}_{-0.20}$

Notes. Line-of-sight velocity dispersion (σ_e) of the two AGNs. The value r_e is the effective radius. The factor $k(n)$ in equation (2) depends on n that is the Sérsic index. The spheroidal masses in logarithmic units of $M_\odot$.

Table 6. Gas-to-dust and M_{SMBH}/M_{Host} ratios.

Object	A_V/N_H	$\log(M_{SMBH}/M_{bulge})$
J00	$\geq 2.61 \times 10^{-21}$	$-2.77^{+0.36}_{-0.34}$
J02	$1.30^{+1.8}_{-1.1} \times 10^{-21}$	-4.15 ± 0.39
Reference value	5.3×10^{-22}	-2.9 ± 0.5

Notes. The units of A_V/N_H are in mag cm^{-2}. The reference value for A_V/N_H is the Galactic and for $\log(M_{SMBH}/M_{bulge})$ is the mean value from Merritt & Ferrarese (2001).

Compton-thick AGNs are expected and known to display large EW Fe K emission lines at 6.4 keV ($\leq$1 keV; Gandhi et al. 2014), due to the highly suppressed underlying continuum. No Fe line is detected by the fits with high significance in any of our sources.

The Compton-thin nature of the sources is supported by the high $L_{2-10\,keV}/L_{[O\,III]}$ ratio, where $L_{[O\,III]}$ is the unreddened luminosity of the [O III] emission line at rest frame λ5007 Å. This is because if we only detect in X-rays the soft scattered component (which is only a few per cent of the intrinsic AGN power), the X-ray luminosity can be largely underestimated. Therefore, we can use $L_{[O\,III]}$ as a proxy of the bolometric luminosity and compare it to the $L_{2-10\,keV}$. Compton-thick sources have $L_{2-10\,keV}/L_{[O\,III]} < 0.1$–1.0 (Bassani et al. 1999; Akylas & Georgantopoulos 2009). This ratio is 69 for J02 and 22 for J00. This effectively excludes the Compton-thick character of both of our sources.

Alternatively, we could use the mid-IR to L_X ratio to identify Compton-thick obscuration (Gandhi et al. 2009; Asmus et al. 2011; Mateos et al. 2015; Stern 2015). If we use the three shortest λ-bands of the *Wide-Field Infrared Survey Explorer* (3.4, 4.6, 6, 12 μm; Wright et al. 2010), we find that our sources have mid-IR colours that fall outside of the region occupied by AGNs (Mateos et al. 2012), because their catalogued fluxes have significant contamination from the AGN hosts.

6.2 Host–SMBH relations

We estimated the SMBH-to-host galaxy mass ratio for our two sources (see Table 6) and we compared them with the value reported by Merritt & Ferrarese (2001), $\langle \log(M_{SMBH}/M_{bulge}) \rangle = -2.9$ with an rms of 0.5 dex. This has been derived by using the samples of bulges and elliptical galaxies of Ferrarese et al. (2001) and Gebhardt et al. (2000). For J00, we obtain $\langle \log(M_{SMBH}/M_{bulge}) \rangle = -2.77$, which is consistent with the Meritt and Ferrarese relation. This means that the galaxy is as massive as expected by its SMBH. J02 has $\langle \log(M_{SMBH}/M_{bulge}) \rangle = -4.15$, that is more than two times the rms below the standard relation. For J02 host galaxy dilution could explain, at least in part, the lack of broad emission line detection in the 6dF spectrum. This is because we expect more impact of the star-light dilution on the AGN emission compared to AGNs with less massive host galaxies. There are many examples in the literature of apparently normal galaxies (e.g. X-ray bright optically normal galaxies) in which, after the host galaxy contamination is removed, AGN emission is revealed (Severgnini et al. 2003; Georgantopoulos & Georgakakis 2005; Caccianiga et al. 2007). In the next sections, we will investigate if this is the only factor that contributes to the observed optical/X-ray discrepancy.

Table 7. AGN optical extinction.

	J00	J02
$A_{V,\,NLR}$	$1.07^{+0.67}_{-0.81}$	$0.30^{+0.77}_{-0.81}$
$A_{V,\,cont.}$	2.04 ± 0.30	2.19 ± 0.33
$A_{V,X-ray}$	≤ 0.05	0.13

Notes. Optical extinction of the NLR and AGN continuum in mag. The NLR extinction is converted through the Balmer decrement (Bassani et al. 1999; Pappa et al. 2001; Carrera, Page & Mittaz 2004) through the expression $E(B-V) = 2.07 \times \log((H\alpha/H\beta)/3)$ and $R_V = 3.1$. The $A_{V,X-ray}$ is the optical extinction corresponding to the N_H column density using the SMC model of Gordon et al. (2003).

6.3 Dust-to-gas ratio of the obscuring medium and Balmer decrement

Typically AGNs have dust-to-gas ratios lower than or compatible with the Galactic value (Maiolino et al. 2001; Vasudevan et al. 2009; Parisi 2011; Marchese et al. 2012; Hao et al. 2013; Burtscher et al. 2016). This result does not appear only in X-ray-selected studies, but also on optical- and IR-selected AGNs (Wilkes et al. 2002; Young, Elvis & Risaliti 2008). We have compared A_V (see Table 7) and N_H (see Table 1) for our sources. For J00 $A_V/N_H \geq 2.61 \times 10^{-21}$ mag cm^{-2}, while for J02 $A_V/N_H = 1.30^{+1.8}_{-1.1} \times 10^{-21}$ mag cm^{-2}. The Galactic relation is $A_V/N_H = 5.3 \times 10^{-22}$ mag cm^{-2}. J00 shows an A_V/N_H more than five times the Galactic value. For J02, the value is consistent with the Galactic. As mentioned in Section 5.1, the SMC extinction model is one of the most conservative measurements on the A_V of all models taken into account. The results provided by the other extinction models do not change the results in terms of the dust-to-gas ratio.

A dust-to-gas ratio higher than the Galactic value explains the observed properties of J00. It is a scenario offered in Panessa & Bassani (2002) to explain the different optical and X-ray classification of unabsorbed Seyfert 2. In this case, a strong contribution of dust has less effect in the X-ray emission than the optical one. There are a few examples in the literature of higher dust-to-gas than the Galactic value (Trippe et al. 2010; Huang et al. 2012; Mehdipour et al. 2012), but this scenario is not very common as it is about 3–9 per cent of the sources (Maiolino et al. 2001; Caccianiga et al. 2004; Malizia et al. 2012).

6.4 Intrinsically weak BLR emission

To investigate whether our AGNs have a BLR with non-standard properties (e.g. underluminous), we have determined the luminosity ratio L_{NLR}/L_{BLR} from the broad and narrow components of the H α emission line (see Table 4). Then, we compare our values with the relation between L_{NLR}/L_{BLR} and L_{BLR} found for AGNs of similar z and luminosities to ours from Stern & Laor (2012). Our objects have L_{NLR}/L_{BLR} ratios within the observed 0.4 dex scatter hence, none of our sources appears to have intrinsically weak BLR.

6.5 Variability

AGNs are highly variable sources across the full electromagnetic spectrum at both long and short time-scales (Ulrich, Maraschi & Urry 1997; Mateos et al. 2007; Krumpe et al. 2010; García-González et al. 2015; Hernández-García et al. 2015; LaMassa et al. 2015). This is originated by variability in the accretion rate and by extinction variability in the line-of-sight material (Markowitz, Krumpe & Nikutta 2014; Miniutti et al. 2014). As the X-ray and UV/optical observations have not been taken simultaneously we cannot rule out that this might also contribute to the observed mismatch between the optical and X-ray properties of our AGNs.

As a check, we carried out the UV-to-optical spectral decomposition into AGNs and host galaxy emission with the public SDSS-DR7 spectrum of J00 (taken in 2000-09-05), using the same broken power law for the AGN emission and the same host galaxy emission from Section 5.1. In this test, we compare the intrinsic flux of the AGN, so we have taken into account that the SDSS spectra were taken with a 3 arcsec fibre and hence a higher fraction of AGNs enters through the fibre and the host galaxy contribution is higher than in the XSHOOTER spectra. Analysing the results there is some variation, that is best fitted by an extinction change ($A_{\rm V,\,SDSS} = 0.69 \pm 0.10$ mag versus the one obtained by XSHOOTER, that is $A_{\rm V,\,XSH} = 2.04 \pm 0.29$ mag) instead of a change in the emission of the AGN. The computed $A_{\rm V}$ gives a higher dust-to-gas ratio than the Galactic ($A_{\rm V}/N_{\rm H} > 8.8 \times 10^{-22}$ mag cm^{-2}), as with the XSHOOTER data. The 6dF optical spectrum of J02 is not of sufficient quality for conducting a spectral decomposition analysis.

We conclude that extinction variability could be present in at least one of the sources (the one with the largest $A_{\rm V}/N_{\rm H}$ ratio). Even so, a higher than Galactic dust-to-gas ratio is also needed in that source. For this source, we only observe a marginal variation of the intrinsic flux of 1.6σ. Simultaneous X-ray and optical observations are needed to assess the actual importance of variability.

7 CONCLUSIONS

In this work, we have investigated the origin of the apparent mismatch of the optical and X-ray classifications of two AGNs with high optical extinction but low X-ray absorption. In our two selected objects, there is a clear broad line in Hα using the data from VLT/XSHOOTER after a careful removal of the host galaxy contribution.

We discussed several scenarios that could explain the discordance of our observations. We ruled out a Compton-thick nature of our sources, on the basis of the $L_{2-10\,\rm keV}/L_{[\rm O\,III]}$ ratio. We also discarded that the total or partial absence of broad lines in the spectrum is caused by an intrinsically weak BLR emission.

The origin of the mismatch for each object is found to be different. An intrinsically different $A_{\rm V}/N_{\rm H}$ is the best explanation for the properties of the object J00 without the need to invoke variability. This obscuring material has a dust-to-gas ratio really different than the majority of the AGN population. The other object, J02, has a massive host galaxy in comparison with its SMBH, so that the broad emission lines and the nuclear continuum are swamped by the host galaxy star light which makes them very difficult to detect.

ACKNOWLEDGEMENTS

We thank the anonymous referee for the comments that have helped us to improve the quality of the manuscript. We thank R. Antonucci and J. Stern for their references and comments that improved our manuscript. IO-P thanks A. Khan-Ali for his support with SHERPA and PYTHON.

IO-P and FJC acknowledge financial support through grant AYA2015-64346-C2-1-P (MINECO/FEDER). SM acknowledges financial support by the Spanish Ministry of Economy and Competitiveness through grant AYA2016-76730-P (MINECO/FEDER). AC, RD, PS and VB acknowledge financial support by the Italian Space Agency (contract ASI-INAF I/037/12/0).

Based on observations obtained with *XMM–Newton*, an ESA science mission with instruments and contributions directly funded by ESA Member States and NASA.

Based on observations collected at the European Organisation for Astronomical Research in the Southern Hemisphere under ESO programme 085.B-0757(A).

This research has made use of the NASA/IPAC Extragalactic Database (NED) that is operated by JPL, Caltech, under contract with the National Aeronautics and Space Administration. The CASSIS is a product of the Infrared Science Center at Cornell University, supported by NASA and JPL.

Funding for the SDSS and SDSS-II has been provided by the Alfred P. Sloan Foundation, the Participating Institutions, the National Science Foundation, the U.S. Department of Energy, the National Aeronautics and Space Administration, the Japanese Monbukagakusho, the Max Planck Society and the Higher Education Funding Council for England. The SDSS web site is http://www.sdss.org/.

The SDSS is managed by the Astrophysical Research Consortium for the Participating Institutions. The Participating Institutions are the American Museum of Natural History, Astrophysical Institute Potsdam, University of Basel, University of Cambridge, Case Western Reserve University, University of Chicago, Drexel University, Fermilab, the Institute for Advanced Study, the Japan Participation Group, Johns Hopkins University, the Joint Institute for Nuclear Astrophysics, the Kavli Institute for Particle Astrophysics and Cosmology, the Korean Scientist Group, the Chinese Academy of Sciences (LAMOST), Los Alamos National Laboratory, the Max-Planck-Institute for Astronomy (MPIA), the Max-Planck-Institute for Astrophysics (MPA), New Mexico State University, Ohio State University, University of Pittsburgh, University of Portsmouth, Princeton University, the United States Naval Observatory and the University of Washington.

IRAF is distributed by the National Optical Astronomy Observatory, which is operated by the Association of Universities for Research in Astronomy (AURA) under cooperative agreement with the National Science Foundation.

The STARLIGHT project is supported by the Brazilian agencies CNPq, CAPES and FAPESP and by the France-Brazil CAPES/Cofecub program.

This publication uses data products from the Two Micron All-Sky Survey, which is a joint project of the University of Massachusetts and the Infrared Processing and Analysis Center/California Institute of Technology, funded by the National Aeronautics and Space Administration and the National Science Foundation.

REFERENCES

Abazajian K. N. et al., 2009, ApJS, 182, 543
Akylas A., Georgantopoulos I., 2009, A&A, 500, 999
Allen C. W., 1973, Astrophysical Quantities, 3rd edn. University of London, Athlone Press
Antonucci R., 1993, ARA&A, 31, 473

Arnaud K. A., 1996, in Jacoby G. H., Barnes J., eds, ASP Conf. Ser. Vol. 101, Astronomical Data Analysis Software and Systems V. Astron. Soc. Pac., San Francisco, p. 17
Asmus D., Gandhi P., Smette A., Honig S. F., Duschl W. J., 2011, A&A, 536, A36
Barcons X., Carrera F. J., Ceballos M. T., 2003, MNRAS, 339, 757
Baron D., Stern J., Poznanski D., Netzer H., 2016, ApJ, 832, 8
Bassani L., Dadina M., Maiolino R., Salvati M., Risaliti G., Della Ceca R., Matt G., Zamorani G., 1999, ApJS, 121, 473
Bell E. F., de Jong R. S., 2001, ApJ, 550, 212
Bianchi S., Corral A., Panessa F., Barcons X., Matt G., Bassani L., Carrera F. J., Jiménez-Bailón E., 2008, MNRAS, 385, 195
Bianchi S. et al., 2012, MNRAS, 426, 3225
Braito V. et al., 2003, A&A, 398, 107
Braito V., Reeves J. N., Sambruna R. M., Gofford J., 2011, MNRAS, 414, 2739
Brightman M., Nandra K., Salvato M., Hsu L.-T., Aird J., Rangel C., 2014, MNRAS, 443, 1999
Bruzual G., Charlot S., 2003, MRAS, 344, 1000
Burtscher L. et al., 2016, A&A, 586, A28
Caccianiga A. et al., 2004 A&A, 416, 901
Caccianiga A., Severgnini P., Della Ceca R., Maccacaro T., Carrera F. J., Page M. J., 2007, A&A, 470, 557
Caccianiga A. et al., 2008, A&A, 477, 735
Calzetti D., Armus L., Bohlin R. C., Kinney A. L., Koornneef J., Storchi-Bergmann T., 2000, ApJ, 533, 682
Cappellari M. et al., 2006, MRAS, 366, 1126
Cardelli J. A., Clayton G. C., Mathis J. S., 1989, ApJ, 345, 245
Carrera F. J., Page M. J., Mittaz J. P. D., 2004, A&A, 420, 163
Cid Fernandes R., Mateus A., Sodré L., Stasińska G., Gomes J. M., 2005, MNRAS, 358, 363
Comastri A., 2004, in Barger A. J., eds, Astrophysics and Space Science Library, Vol. 308, Supermassive Black Holes in the Distant Universe. Kluwer, Dordrecht, p. 245
Corral A., Della Ceca R., Caccianiga A., Severgnini P., Brunner H., Carrera F. J., Page M. J., Schwope A. D., 2011, A&A, 530, A42
Corral A., Georgantopoulos I., Watson M. G., Rosen S. R., Page K. L., Webb N. A., 2015, A&A, 576, A61
de Vaucouleurs G., de Vaucouleurs A., Corwin H. G., Jr, Buta R. J., Paturel G., Fouqué P., 1991, Third Reference Catalogue of Bright Galaxies. Springer, New York
Del Moro A. et al., 2016, MNRAS, 456, 2105
Della Ceca R., Pellegrini S., Bassani L., Beckmann V., Cappi M., Palumbo G. G. C., Trinchieri G., Wolter A., 2001, A&A, 375, 781
Dickey J. M., Lockman F. J., 1990, ARA&A, 28, 215
Ferrarese L., Merritt D., 2000, ApJ, 539, L9
Freeman P., Doe S., Siemiginowska A., 2001, in Starck J.-L., Murtagh F. D., eds, Proc. SPIE Conf. Ser. Vol. 4477, Astronomical Data Analysis. SPIE, Bellingham, p. 76
Galbiat E. et al., 2005, A&A, 430, 927
Gandhi P., Horst H., Smette A., Honig S., Comastri A., Gilli R., Vignali C., Duschl W., 2009, A&A, 502, 457
Gandhi P. et al., 2014, ApJ, 792, 117
García-González J., Alonso-Herrero A., Pérez-González P. G., Hernán-Caballero A., Sarajedini V. L., Villar V., 2015, MNRAS, 446, 3199
Gaskell C. M., Goosmann R. W., 2013, ApJ, 769, 30
Gebhardt K. et al., 2000, ApJ, 539, L13
Georgantopoulos I., Georgakakis A., 2005, MNRAS, 358, 131
Georgantopoulos I., Rovilos E., Xilouris E. M., Comastri A., Akylas A., 2011a, A&A, 526, A86
Georgantopoulos I. et al., 2011b, A&A, 534, 23
Gilli R., Salvati M., Hasinger G., 2001, A&A, 366, 407
Gordon K. D., Clayton G. C., Misselt K. A., Landolt A. U., Wolff M. J., 2003, ApJ, 594, 279
Greene J. E., Ho L. C., 2005, ApJ, 630
Hao H. et al., 2013, MNRAS, 434, 4, 3104
Hernández-García L., Masegosa J., González-Martín O., Márquez I., 2015, A&A, 579, A90
Hopkins P. F. et al., 2004, AJ, 128, 1112
Huang X., Wang J., Tan Y., Yang H., Huang Y., 2011, ApJ, 734, L16
Jansen F. et al., 2001, A&A, 365, 1, L1
Jones D. H. et al., 2009, MNRAS, 399, 683
Kaastra J. S., 1992, An X-Ray Spectral Code for Optically Thin Plasmas. SRON-Leiden Internal Report
Kaspi S., Smith P. S., Netzer H., Maoz D., Jannuzi B. T., Giveon U., 2000, ApJ, 533, 631
Koratkar A., Blaes O., 1999, PASP, 111, 1
Krumpe M., Lamer G., Markowitz A., Corral A., 2010, ApJ, 725, 2444
LaMassa S. et al., 2015, ApJ, 800, 144
Liedahl D. A., Osterheld A. L., Goldstein W. H., 1995, ApJ, 438, L115
López S. et al., 2016, A&A, 594, A91
Mainieri V. et al., 2005, A&A, 437, 805
Maiolino R., Marconi A., Salvati M., Risaliti G., Severgnini P., Oliva E., La Franca F., Vanzi L., 2001, A&A, 365, 28
Malizia A., Bassani L., Bazzano A., Bird A. J., Masetti N., Panessa F., Stephen J. B., Ubertini P., 2012, MNRAS, 426, 1750
Marchese E., Della Ceca R., Caccianiga A., Severgnini P., Corral A., Fanali R., 2012, A&A, 539, A48
Markowitz A. G., Krumpe M., Nikutta R., 2014, MNRAS, 439, 1403
Masetti N. et al., 2012, A&A, 538, A123
Mateos S. et al., 2005a, A&A, 433, 855
Mateos S., Barcons X., Carrera F. J., Ceballos M. T., Hasinger G., Lehmann I., Fabian A. C., Streblyanska A., 2005b, A&A, 444, 79
Mateos S., Barcons X., Carrera F. J., Page M. J., Ceballos M. T., Hasinger G., Fabian A. C., 2007, A&A, 473, 105
Mateos S., Saxton R. D., Read A. M., Sembay S., 2009, A&A, 496, 879
Mateos S. et al., 2010, A&A, 510, A35
Mateos S. et al., 2012, MNRAS, 426, 3271
Mateos S. et al., 2015, MNRAS, 449, 1422
Mateus A., Sodré L., Cid Fernandes R., Stasińska G., Schoenell W., Gomes J. M., 2006, MNRAS, 370, 721
Mehdipour M., Branduardi-Raymont G., Page M. J., 2012, A&A, 542, A30
Merloni A. et al., 2014, MNRAS, 437, 3550
Merritt D., Ferrarese L., 2001, MNRAS, 320, 30
Mewe R., Gronenschild E. H. B. M., van den Oord G. H. J., 1985, A&AS, 62, 197
Mewe R., Lemen J. R., van den Oord G. H. J., 1986, A&AS, 65, 511
Miniutti G. et al., 2014, MNRAS, 437, 1776
Nisini B., Giannini T., Antoniucci S., Alcalá J. M., Bacciotti F., Podio L., 2016, A&A, 595, A76
Page M. J., Carrera F. J., Stevens J. A., Ebrero J., Blustin A. J., 2011, MNRAS, 416, 2792
Panessa F., Bassani L., 2002, A&A, 394, 435
Panessa F., Bassani L., Cappi M., Dadina M., Barcons X., Carrera F. J., Ho L. C., Iwasawa K., 2006, A&A, 455, 173
Pappa A., Georgantopoulos I., Stewart G. C., Zezas A. L., 2001, MNRAS, 326, 995
Parisi P., 2011, PhD Thesis, Univ. di Bologna
Park D., Kelly B. C., Woo J., Treu T., 2012, ApJS, 203, 6
Polletta M. et al., 2007, ApJ, 663, 81
Schmidt K. B., Rix H.-W., Shields J. C., Knecht M., Hogg D. W., Maoz D., Bovy J., 2012, ApJ, 744, 147
Scott A. E., Stewart G. C., Mateos S., 2012, MNRAS, 423, 2633
Severgnini P. et al., 2003, A&A, 406, 483
Spiniello C., Trager S. C., Koopmans L. V. E., Chen Y. P., 2012, ApJ, 753, L32
Steinhardt C. L. et al., 2012, ApJ, 759, 24
Stern D., 2015, ApJ, 807, 129
Stern J., Laor A., 2012, MNRAS, 426, 2703
Strüder L. et al., 2001, A&A, 365, L18
Sulentic J. W., Marziani P., Dultzin-Hacyan D., 2000, ARA&A, 38, 521
Taylor E. N., Franx M., Brinchmann J., van der Wel A., van Dokkum P. G., 2010, ApJ, 722, 1
Tozzi P. et al., 2006, A&A, 451, 457
Trippe S., 2015, J. Korean Astron. Soc., 48, 203

Trippe M. L., Crenshaw D. M., Deo R. P., Dietrich M., Kraemer S. B., Rafter S. E., Turner T. J., 2010, ApJ, 725, 1749
Turner M. J. L. et al., 2001, A&A, 365, L27
Ulrich M. H., Maraschi L., Urry C. M., 1997, ARA&A, 35, 445
Urry C. M., Padovani P., 1995, PASP, 107, 803
van Dokkum P. G., 2001, PASP, 113, 1420
Vasudevan R. V., Mushotzky R. F., Winter L. M., Fabian A. C., 2009, MNRAS, 399, 1553
Vernet J. et al., 2011, A&A, 536, A105
Vitale M. et al., 2013, A&A, 556, A11
Watson M. G. et al., 2009, A&A, 493, 339
Wilkes B. J., Schmidt G. D., Cutri R. M., Ghosh H., Hines D. C., Nelson B., Smith P. S., 2002, ApJ, 564, 65
Winter L. M., Mushotzky R. F., Tueller J., Markwardt C., 2008, ApJ, 674, 2
Wright E. L. et al., 2010, AJ, 140, 1868
Young M., Elvis M., Risaliti G., 2008, ApJ, 688, 128

This paper has been typeset from a TEX/LATEX file prepared by the author.